



Large area optical mapping of surface contact angle

GUILHERME DUTRA,^{1,6} JOHN CANNING,^{1,2,3,7} WHAYNE PADDEN,² CICERO MARTELLI,^{1,4} AND SVETLANA DLIGATCH⁵

¹Graduate School on Electrical Engineering and Applied Computer Science, Federal University of Technology - Paraná, Curitiba, 80230-901 Brazil

²interdisciplinary Photonics Laboratories (iPL), School of Electrical and Data Engineering, The University of Technology, Sydney, NSW 2007, Australia and School of Chemistry, The University of Sydney, NSW 2006, Australia

³Australian Sensor and Identification Systems, Sydney, NSW 2000, Australia

⁴Department of Electronics, Federal University of Technology - Paraná, Curitiba, 80230-901 Brazil

⁵CSIRO Manufacturing, PO Box 218, Lindfield, NSW 2070, Australia

⁶gdutra@alunos.utfpr.edu.br

⁷john.canning@uts.edu.au

Abstract: Top-down contact angle measurements have been validated and confirmed to be as good if not more reliable than side-based measurements. A range of samples, including industrially relevant materials for roofing and printing, has been compared. Using the top-down approach, mapping in both 1-D and 2-D has been demonstrated. The method was applied to study the change in contact angle as a function of change in silver (Ag) nanoparticle size controlled by thermal evaporation. Large area mapping reveals good uniformity for commercial Aspen paper coated with black laser printer ink. A demonstration of the forensic and chemical analysis potential in 2-D is shown by uncovering the hidden CsF initials made with mineral oil on the coated Aspen paper. The method promises to revolutionize nanoscale characterization and industrial monitoring as well as chemical analyses by allowing rapid contact angle measurements over large areas or large numbers of samples in ways and times that have not been possible before.

© 2017 Optical Society of America

OCIS codes: (110.2960) Image analysis; (170.0110) Imaging systems; (240.5770) Roughness; (240.6700) Surfaces; (999.9999) Wettability; (999.9999) Surface mapping.

References and links

1. E. Nowak, G. Combes, E. H. Stitt, and A. W. Pacey, "A comparison of contact angle measurement techniques applied to highly porous catalyst supports," *Powder Technol.* **233**, 52–64 (2013).
2. M. K. Seely, "Irregular fog as a water source for desert dune beetles," *Oecologia* **42**(2), 213–227 (1979).
3. S. Ioppolo, H. M. Cuppen, and H. Linnartz, "Surface formation routes of interstellar molecules: hydrogenation reactions in simple ices," *Rend. Lincei* **22**(3), 211–224 (2011).
4. C. Ladiges, "Aussie innovation helps hunt down gravitational waves," <https://www.csiro.au/en/News/News-releases/2016/Aussie-innovation-helps-hunt-down-gravitational-waves>.
5. CO.FO.ME.GRA., "Quality control in the printing industry," http://www.cofomegra.it/www.cofomegra.it/documents/QUALITY_CONTROLS.pdf.
6. J. Canning, H. Weil, M. Naqshbandi, K. Cook, and M. Lancry, "Laser tailoring surface interactions, contact angles, drop topologies and the self-assembly of optical microwires," *Opt. Mater. Express* **3**(2), 284 (2013).
7. M. Chaplin, "Do we underestimate the importance of water in cell biology?" *Nat. Rev. Mol. Cell Biol.* **7**(11), 861–866 (2006).
8. X. Wang and R. A. Weiss, "A facile method for preparing sticky, hydrophobic polymer surfaces," *Langmuir* **28**(6), 3298–3305 (2012).
9. G. Jiang, Y. Li, and M. Zhang, "Evaluation of gas wettability and its effects on fluid distribution and fluid flow in porous media," *Petrol. Sci.* **10**(4), 515–527 (2013).
10. M. Xu and H. Dehghanpour, "Advances in understanding wettability of gas shales," *Energy Fuels* **28**(7), 4362–4375 (2014).
11. A. Hofmann, C. Kaufmann, M. Müller, and T. Hanemann, "Interaction of high flash point electrolytes and PE-based separators for Li-ion batteries," *Int. J. Mol. Sci.* **16**(9), 20258–20276 (2015).
12. B. H. P. Cheong, T. W. Ng, Y. Yu, and O. W. Liew, "Using the meniscus in a capillary for small volume contact

- angle measurement in biochemical applications,” *Langmuir* **27**(19), 11925–11929 (2011).
13. A. Saghafi, H. Javanmard, and K. Pinetown, “Study of coal gas wettability for CO₂ storage and CH₄ recovery,” *Geofluids* **14**(3), 310–325 (2014).
 14. P. Zhang, M. T. Tweheyo, and T. Austad, “Wettability alteration and improved oil recovery by spontaneous imbibition of seawater into chalk: Impact of the potential determining ions Ca²⁺, Mg²⁺, and SO₄²⁻,” *Colloids Surfaces A Physicochem. Eng. Asp.* **301**(1-3), 199–208 (2007).
 15. A. Borruto, G. Crivellone, and F. Marani, “Influence of surface wettability on friction and wear tests,” *Wear* **222**(1), 57–65 (1998).
 16. T. D. Blake, “The physics of moving wetting lines,” *J. Colloid Interface Sci.* **299**(1), 1–13 (2006).
 17. X. Men, X. Shi, B. Ge, Y. Li, X. Zhu, Y. Li, and Z. Zhang, “Novel transparent, liquid-repellent smooth surfaces with mechanical durability,” *Chem. Eng. J.* **296**, 458–465 (2016).
 18. Z. Zheng, O. Azzaroni, F. Zhou, and W. T. S. Huck, “Topography printing to locally control wettability,” *J. Am. Chem. Soc.* **128**(24), 7730–7731 (2006).
 19. H. Liu, L. Feng, J. Zhai, L. Jiang, and D. Zhu, “Reversible wettability of a chemical vapor deposition prepared ZnO film between superhydrophobicity and superhydrophilicity,” *Langmuir* **20**(14), 5659–5661 (2004).
 20. O. S. Hung, V. Thiyagarajan, and P. Y. Qian, “Preferential attachment of barnacle larvae to natural multi-species biofilms: Does surface wettability matter?” *J. Exp. Mar. Biol. Ecol.* **361**(1), 36–41 (2008).
 21. B. M. Colosimo, F. Mammarella, and S. Petrò, “Quality control of manufactured surfaces,” in *Frontiers in Statistical Quality Control 9*, H.-J. Lenz, P.-T. Wilrich, and W. Schmid, eds. (Physica-Verlag HD, 2010), pp. 55–70.
 22. F. Bottiglione and G. Carbone, “An effective medium approach to predict the apparent contact angle of drops on super-hydrophobic randomly rough surfaces,” *J. Phys. Condens. Matter* **27**(1), 015009 (2015).
 23. A. Nakajima, K. Hashimoto, T. Watanabe, K. Takai, G. Yamauchi, and A. Fujishima, “Transparent Superhydrophobic Thin Films with Self-Cleaning Properties,” *Langmuir* **16**(17), 7044–7047 (2000).
 24. M. Rauscher and S. Dietrich, “Wetting phenomena in nanofluidics,” *Annu. Rev. Mater. Res.* **38**(1), 143–172 (2008).
 25. M. G. Pollack, R. B. Fair, and A. D. Shenderov, “Electrowetting-based actuation of liquid droplets for microfluidic applications,” *Appl. Phys. Lett.* **77**(11), 1725–1726 (2000).
 26. W. Wang and A. Gupta, “Investigation of the effect of temperature and pressure on wettability using modified pendant drop method,” in *SPE Annual Technical Conference and Exhibition* (Society of Petroleum Engineers, 1995), pp. 117–126.
 27. P. G. de Gennes, “Wetting: statics and dynamics,” *Rev. Mod. Phys.* **57**(3), 827–863 (1985).
 28. D. Quéré, “Wetting and roughness,” *Annu. Rev. Mater. Res.* **38**(1), 71–99 (2008).
 29. R. Soref, “The past, present, and future of silicon photonics,” *IEEE J. Sel. Top. Quantum Electron.* **12**(6), 1678–1687 (2006).
 30. D. Bonneau, J. W. Silverstone, and M. G. Thompson, *Silicon Quantum Photonics*, in L. Pavesi and J. D. Lockwood, eds. (Springer Berlin Heidelberg, 2016), pp. 41–82.
 31. J. Canning, “Birefringence control in planar waveguides using doped top layers,” *Opt. Commun.* **191**(3-6), 225–228 (2001).
 32. J. Lai, B. Sunderland, J. Xue, S. Yan, W. Zhao, M. Folkard, B. D. Michael, and Y. Wang, “Study on hydrophilicity of polymer surfaces improved by plasma treatment,” *Appl. Surf. Sci.* **252**(10), 3375–3379 (2006).
 33. C. C. Dupont-Gillain, B. Nysten, V. Hlady, and P. G. Rouxhet, “Atomic force microscopy and wettability study of oxidized patterns at the surface of polystyrene,” *J. Colloid Interface Sci.* **220**(1), 163–169 (1999).
 34. W. C. Bigelow, D. L. Pickett, and W. A. Zisman, “Oleophobic monolayers,” *J. Colloid Sci.* **1**(6), 513–538 (1946).
 35. G. L. Mack, “The determination of contact angles from measurements of the dimensions of small bubbles and drops: The spheroidal segment method for acute angles,” *J. Phys. Chem.* **40**(2), 159–167 (1935).
 36. J. Järnström, B. Granqvist, M. Jäm, C. M. Tåg, and J. B. Rosenholm, “Alternative methods to evaluate the surface energy components of ink-jet paper,” *Colloids Surfaces A Physicochem. Eng. Asp.* **294**(1-3), 46–55 (2007).
 37. D. Kwok and A. Neumann, “Contact angle interpretation in terms of solid surface tension,” *Colloids Surfaces A Physicochem. Eng. Asp.* **161**(1), 31–48 (2000).
 38. C. J. Van Oss, R. J. Good, and M. K. Chaudhury, “Additive and nonadditive surface tension components and the interpretation of contact angles,” *Langmuir* **4**(4), 884–891 (1988).
 39. A. Satyaprasad, V. Jain, and S. K. Nema, “Deposition of superhydrophobic nanostructured Teflon-like coating using expanding plasma arc,” *Appl. Surf. Sci.* **253**(12), 5462–5466 (2007).
 40. B. Arkles, “Hydrophobicity, hydrophilicity and silanes,” *Paint Coatings Ind.* 114 (2006).
 41. B. R. Ray and F. E. Bartell, “Hysteresis of contact angle of water on paraffin. Effect of surface roughness and of purity of paraffin,” *J. Colloid Sci.* **8**(2), 214–223 (1953).
 42. C. S. Wojtysiak, “Radiative cooling surface coatings,” U.S. patent US7503971 B2 (2009).
 43. SkyCool Pty Ltda, “SkyCool,” (2016).
 44. J. Canning, “Smartphone spectrometers and other instrumentation,” *SPIE Newsroom*, 42–44 (2016).
 45. M. Arafat Hossain, J. Canning, S. Ast, K. Cook, P. J. Rutledge, and A. Jamalipour, “Combined “dual” absorption and fluorescence smartphone spectrometers,” *Opt. Lett.* **40**(8), 1737–1740 (2015).
 46. M. A. Hossain, J. Canning, K. Cook, and A. Jamalipour, “Smartphone laser beam spatial profiler,” *Opt. Lett.*

- 40(22), 5156–5159 (2015).
47. M. A. Hossain, J. Canning, S. Ast, P. J. Rutledge, and A. Jamalipour, “Early warning smartphone diagnostics for water security and analysis using real-time pH mapping,” *Photonic Sensors* **5**(4), 289–297 (2015).
48. J. Canning, A. Lau, M. Naqshbandi, I. Petermann, and M. J. Crossley, “Measurement of fluorescence in a rhodamine-123 doped self-assembled “giant” mesostructured silica sphere using a smartphone as optical hardware,” *Sensors (Basel)* **11**(12), 7055–7062 (2011).

1. Introduction

Surface properties are fundamental to interactions since they occur within the nanoscale interface region of a surface and an interacting species – they are at the core of material science whether they are surfaces on nanoparticles used to make catalysis more efficient [1] or vast expansive surfaces such as those used to collect water from fog [2]. The bulk of a medium is generally irrelevant if there is no surface for interaction to occur and a great deal of chemical engineering is spent working around increasing surface area to volume to maximize efficiencies to make processes not only useful but also viable. However, even the surfaces themselves reveal information about the underlying molecular physics of its structure and its formation. The nanoscale interfaces at the heart of surface interactions with a range of species having their own molecular-sized to very large surfaces, are also vital in establishing the quality of a surface in dimensions that are many orders of magnitude larger. In deep space molecular surfaces scale to have vast interactions across almost unfathomable dimensions [3]. On earth the search for gravitational waves required LIGO mirror coatings with almost unfathomable surface homogeneity [4] and paper for the printing and food sectors demands uniform paper surface properties, at least within an acceptable range defined by quality assurance [5]. It is no small statement to suggest that interfaces are at the heart of science and engineering.

A key parameter used in chemistry and chemical engineering for understanding nanoscale surface interactions and properties involving solutions across larger areas is wettability, or the property of a material to attract or repel a solvent, which manifests itself on its ability to spread, or adhere to, a solid surface. A macro definition of this sort allows one to bypass much of the individual molecular aspects of a surface taking into account the role of surface topology in affecting interactions. Thus the degree of chemical attraction, or omniphilicity can be altered to produce repulsion, or omniphobicity, by simply altering surface properties perhaps using laser radiation [6]. This topological behavior is, arguably, an example of emergent phenomena that are not obvious to predict from the molecular scale. Similarly, characteristics of an interacting solvent can produce behavior that may not be exactly that predicted from its molecular constituents and the surface alone. Water is an example where intermolecular forces and dipole orientation produce collective behavior at interfaces that are fundamental to human life but which would not otherwise occur [7]. Thus it is possible to see that whilst clearly there is great complexity in detail involved with exact descriptions of interfacial interactions, the collective description of wettability can play a greater role in attributing a common language that can make the study of such interfaces solvable. The wettability of a surface can provide important information concerning the surface as a whole, both in terms of physical and chemical properties including adhesion forces, free energies associated with adhesion, surface tensions, dipole alignment and much more. These are typical parameters used in understanding, for example, polymer stickiness arising from textured surfaces to various solvents [8]. Wettability is a macroscopic parameter along a nanoscale interface and describes adsorption and repulsion of molecules at interfaces. These interfaces themselves may be involve gas-gas, liquid-gas, liquid-liquid, solid-liquid and solid-solid interactions, variation of which have industrial importance to sectors such as the oil and gas industries [9,10] and batteries [11]. The most common case typically involves solid-liquid interactions. Wetting and the associated forces it generates are responsible for other important effects, including capillary flow [12].

Overall, many industrial processes are enhanced by characterizing and understanding wettability. Wettability plays a crucial role in many applications including oil recovery within the oil and gas sectors [13,14], improving lubricants [15], liquid coatings [16], water and oil repellent surfaces [17], and for quality control within the printing industry [18]. Research laboratories, both public and industrial, use wettability to determine changes on surfaces arising from chemical reactions [19], the attachment of species [20] and to develop new approaches, both chemical and physical, to control surfaces [21]. Superhydrophobic surfaces [22] are increasingly popular for applications in self-cleaning [23], nano-fluidics [24], and electro-wetting [25].

To this end, quantification using solvent droplets sufficiently small that surface tension can resist deformation by gravity, can easily be made independent of detail – the contact angle measures the angle degree of affinity of a solvent to a surface. Contact angle measurements are routine within laboratories for ascertaining surface properties, involving a simple microscopic image of a small spherical-shaped caplet drop from the side and fitting a tangent where it meets the surface. When the contact angle, $\theta < 90^\circ$, the surface is attractive or omniphilic (hydrophilic for water, lipophilic for non-water solvents), when it is greater and repulsion dominates it is omniphobic (hydrophobic for water, lipophobic for non-water solvents) when repulsion dominates. Above $\theta = 150^\circ$, the surface is superomniphobic (or superhydrophobic and superlipophobic). Given the nature of wettability it is clear that a range of factors can affect the contact angle including temperature, pressure, gravity and roughness [26–28]. Contact angle has become the default bench mark tool for ascertaining solid-liquid interfaces within a laboratory. Unfortunately, what appears to be at first glance a relatively simple technique to implement for any competent laboratory experimentalist and is consequently used widely, suffers from a range of practical challenges. Standardized equipment available commercially is surprisingly expensive; the simple side-imaging method also belies significant challenges in illumination and drop positioning where typically it needs to be placed close to an edge for reference. Drop size, which varies with solvent, must be small enough so that gravity does not distort measurements – this in turn can make adjustments in side illumination awkward and contact angle extractions using a tangent subject to some variation. Contact angle measurements can be operator sensitive and resolution and accuracy limited as well as confined to one off-measurements. More significantly, for many applications it is not obvious that a measurement on the edge of a surface is a true representation of surface properties at the center or elsewhere. For example, a silica-silicon wafer typically used for optoelectronic and photonic circuits [29,30], is highly stressed as a result of bimaterial strains [31], itself a solid-solid surface phenomenon arising from both molecular and thermal coefficient mismatch. That strain is not uniform and differs greatly from the outside in, often leading to warping of the wafer.

For these reasons, whilst contact angles are used in industry to provide some laboratory assessment, other methods are employed. These rely on more direct surface measurements using high resolution, large infrastructure such as scanning electronic microscopic (SEM) [32] and atomic force microscopy (AFM) [33], with all the obvious disadvantages they bring including expense, time, coating procedures that damage a sample and more. By focusing on such high resolution measurements, these methods can also fail to properly capture emergent properties on scales well beyond the nano that are more relevant to an industrial process. It is almost certainly a reason why simple contact angle apparatus, which provides a nanoscale interface measurement over an orthogonally large area, sold commercially can build an argument for high cost based on providing a reliable but quick measurement.

Despite the significance of wettability and surface interactions across research and industry, it is one of the most striking problems of today that there exists no measurement tool to map surface properties on any scale without prohibitive access and time frames. Whilst there has been much focus on novel nanoscale and sub-nanoscale measurements using increasingly expensive next generation infrastructure, the inability to span long scales exposes

a serious gap in practical nano-research that remains largely unaddressed. It is a large gap that must be addressed if industrial quality control and research expediency is to keep up with local measurements. In this paper we address this limitation and demonstrate how contact angle can be extended and applied to map the properties of surfaces over large areas, building up surface wettability maps (SWM) that can form the basis for detailed and through control of both research and industrial methods. We apply this to a range of surfaces, focusing in particular on the laser-printing sector where quality control of silica coated paper is critical to high quality printing. To test the resolution of the approach, we characterize a silver-coated slide where the silver is dispersed in particle-like patterns, sizes varying from one end to the other. We also provide a simple demonstration of how contact angle can be used to identify the presence of a sample on a surface, a potential chemical forensic approach.

2. Results

2.1 Top-down contact angle measurements

Contact angle measurements are usually performed from the side. To avoid deformation due to gravity, which can distort the drop shape and therefore the contact angle, the volume should be sufficiently small to ensure the surface tension is higher than the gravitational force. Typically, the angle is then extracted by measuring the tangent to the surface where the drop surface and air meet [34], ostensibly known as the “tangent method”, although other methods, such as the spheroidal segment method, have been described and are sometimes used [35,36]. As noted earlier, the requirement for a side measurement is a serious impediment for mapping surfaces since the drop can only be positioned within the focal range of an imaging lens near the surface edge. A potentially simpler technique that can allow mapping is to undertake top-down measurements of contact angle – given the geometric nature of the spherical caplet it should be possible to extract the contact angle directly from measurements of the drop based diameter itself. Since the method now calculates contact angle from drop diameters, rather than direct side measurement, many of the constraints of side measurement are removed. For example, the method is expected to be more robust to surface tilt where the diameter on a hydrophilic surface remains unchanged for small tilts even as the drop shape slightly distorts producing different angles when measured from either side of the drop. This section describes the top-down approach and a detailed study comparing it with both side measurement approaches.

At the triple phase point of a solid surface, a liquid drop and air the energies describing surface tensions at each of the three interfaces lead to net equilibrium characterized by a unique contact angle, θ . This equilibrium contact angle can therefore be calculated from each of the interface energies, described in Young's equation [37]:

$$\gamma_{SG} - \gamma_{SL} - \gamma_{LG} \cos \theta = 0. \quad (1)$$

Since the adhesion is described by the solid-liquid interface energy, and assuming similar energies for both solid-gas and liquid-gas interfaces, θ can also be related to the adhesion energy:

$$\gamma(1 + \cos \theta) = \Delta W_{SLM}, \quad (2)$$

where ΔW_{SLM} is the solid/liquid adhesion energy per unit area on the medium M . This is the Young-Dupré equation [37].

The optical measurement of θ for a sessile drop is typically made by lateral side imaging using microscope lens-camera system. This measurement requires care given in most cases the drop needs to be near a well-defined reference edge such as a sample slide, for example. The tangent method involves directly drawing the tangent on the drop image and therefore measuring the contact angle. Whilst many image software packages have the ability to directly draw angles and tangents to simplify this process, the fitting is done by the operator

and can lead to errors in angle of about 1 to 2°, made worse when the imaging and illumination is not consistent. Figure 1 illustrates schematically the side methods. Figures 1(a) and 1(b) show the omniphilic and omniphobic images, respectively, where the tangent and corresponding contact angle are measured directly. Given that for accuracy the drop must be as small as is feasible to null out deformation from gravity, it is also possible to indirectly extract θ from the dimensions of a spherical caplet. Figures 1(c) and 1(d) show, respectively, omniphilic and omniphobic images of the fractional sphere with measurements of the height, h , and caplet base diameter, d_{cap} , or caplet base radius, r_{cap} , of a drop. The contact angle can be readily extracted:

$$\theta = 2 \tan^{-1} \frac{h}{r_{cap}} = 2 \tan^{-1} \frac{2h}{d_{cap}}. \quad (3)$$

This is the basis of the spheroidal segment method [35,36].

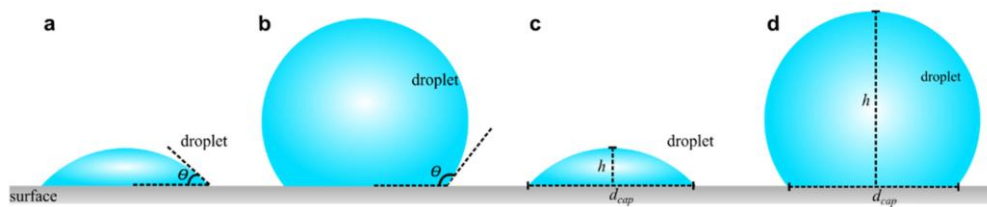


Fig. 1. Schematic for representation of the tangent method for (a) omniphilic and (b) omniphobic surfaces; the spheroidal segment (or height-diameter) method for (c) omniphilic and (d) omniphobic surfaces.

What distinguishes a top-down approach is that the imaging is carried out from the top – immediately it has none of the problems associated with the side view approach and the potential for mapping becomes clear. There are some complications, however, in that the omniphilic and omniphobic situations can be less than clear. In general, for omniphilic surface d_{cap} (or r_{cap}) is easily measured from the upper image as shown by the circular area in Fig. 2(a). For omniphobic surfaces, the sphere diameter d (or radius r) of the equivalent full spherical drop can be directly measured (the circular area in Fig. 2(b). This then needs to be correlated to r_{cap} since the variables r , h and r_{cap} are mutually dependent. Hence, by applying simple Pythagorean Theorem r_{cap} can be defined as:

$$r_{cap}^2 = 2rh - h^2, \quad (4)$$

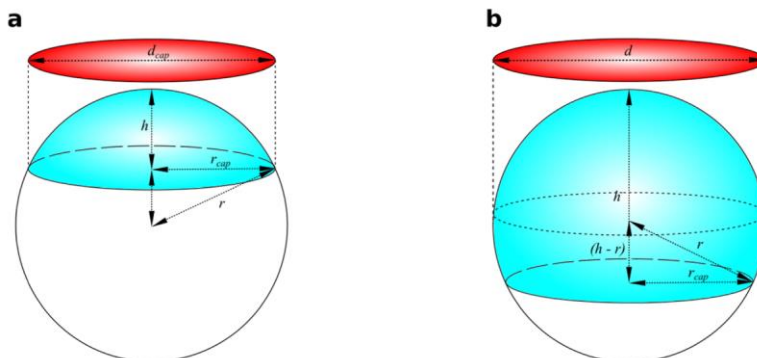


Fig. 2. Schematic drawings of the top-down method for (a) omniphilic and (b) omniphobic surfaces.

Another important parameter for the top-down method is volume V of the drop, which can be controlled experimentally. Both the height h and radius r_{cap} of the spherical cap can be correlated to the volume V of the drop:

$$V = \frac{\pi h}{6} (3r_{cap}^2 + h^2), \quad (5)$$

reorganizing as a function of the drop height, h , leads to a cubic Eq. (6):

$$\frac{1}{6} \pi h^3 + \frac{1}{2} \pi r_{cap}^2 h - V = 0, \quad (6)$$

Values for r_{cap} and h can therefore be obtained using Eqs. (4) and (6). These can then be inserted into Eq. (3) to numerically determine the contact angle θ . For practical implementation, (6) can be made non-dimensional using the following ratio substitutions:

$$H = \frac{h}{r}; \quad (7)$$

$$V_r = \frac{V}{\left(\frac{4}{3} \pi r^3\right)}. \quad (8)$$

These leads to the dimensionless cubic:

$$H^3 - 3H^2 + 4V_r = 0. \quad (9)$$

The dimensionless variable, V_r , represents the volume ratio of the actual volume of the drop to a fully spherical drop with the same measured radius r . Using software, such as Mathematica, to solve the Eq. (9) analytically for H , three possible solutions are obtained. However, only one of these roots is physical: i.e. produces a value of H lying in the range $0 \leq H \leq 2$. An alternative form for the contact angle that is readily derived from Fig. 2 is therefore given by:

$$\theta = \tan^{-1} \frac{r_{cap}}{r-h} \equiv \tan^{-1} \frac{\sqrt{2H-H^2}}{1-H}, \quad (10)$$

where Eqs. (4) and (7) has been used to transform the result. Substituting the analytical solution for H into Eq. (9) and plotting the result as a function of V_r results for the omniphilic ($0 < V_r < 0.5$), and omniphobic ($0.5 < V_r < 1$) cases, shown in Fig. 3A and B. These plots allow one to simply lookup the contact angle using the measured data and the calculated volume ratio V_r . A summary of the procedure used to measure parameters and calculate contact angle with the top-down approach is given in the methods section.

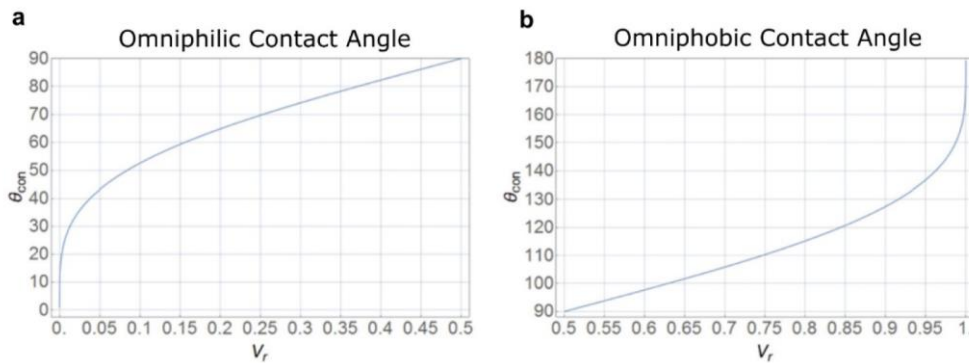


Fig. 3. Plots of the contact angle θ_{con} for drops on both (a) omniphilic and (b) omniphobic surfaces calculated using the top-down method. Contact angle is plotted as a function of the volume ratio V_r .

To experimentally validate the top-down approach a comparison with the other two tangent and spherical segment side measurements was carried out for drops of water on a range of both hydrophilic and hydrophobic surfaces – the results are summarized in Table 1. Both side and top-down measurements were undertaken simultaneously using two portable Dino-lite mini-microscope imaging cameras, the details described in the methods section. Measurements were repeated five times each for each surface and each method to ensure reproducibility; these were also carried out for varying drop sizes and the average readings are shown. Teflon (a polytetrafluoroethylene based polymer) and silane coated slides and surfaces of different materials, including propriety industrial coating films for roofing, silica, polymer parafilm and laser printing papers with and without coatings were examined. The methods were also compared for different drop sizes to assess reproducibility and reliability.


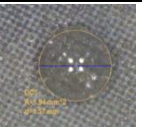
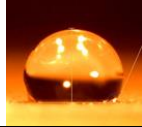
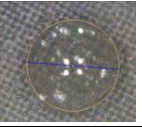


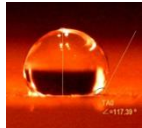
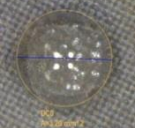



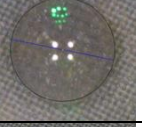
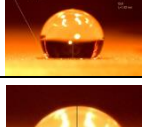
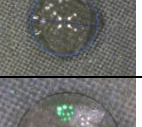
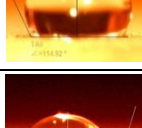
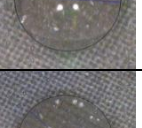
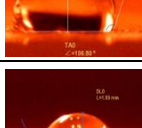
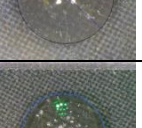


Microscopic examination reveals the pyramidal-like periodic structure (pitch, $\lambda \sim 140 \mu\text{m}$, varying somewhat between samples) of the Teflon coated samples which gives rise to its hydrophobicity, measured as $\theta \sim (106-115)^\circ$, in agreement with the broader literature where $\theta \sim (104-118)^\circ$ [25,38,39], depending on the nature of the Teflon. The contact angle is observed to increase to a maximum as the drop volume increases up to $5 \mu\text{L}$ before beginning to decrease again, suggesting nonlinear changes in balance between drop surface tensions and gravity as the mass increases. Surface features are clearly important and can greatly enhance this into the super hydrophobic domain if the dimensions are optimized [39].


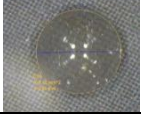


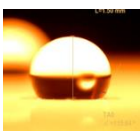
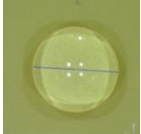
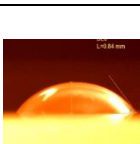

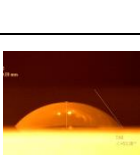
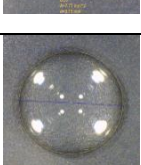
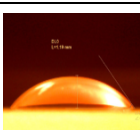

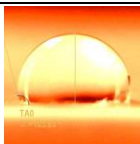
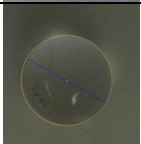

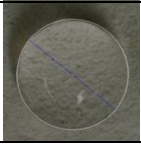
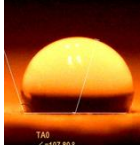

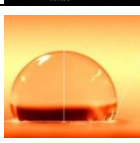
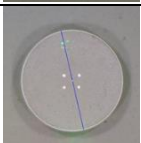
The commercially available silane coated slides with a contact angle $\theta \sim 53-56^\circ$ are hydrophilic, which is surprisingly low as these are typically hydrophobic $\theta \sim (90-110)^\circ$ [40]. Interestingly, one slide had a roughened area which was hydrophobic with a contact angle $\theta \sim (115-117)^\circ$, larger but more consistent with typical values. Whilst direct comparisons are not always possible without more compositional information, this again reflects the importance of structural features in determining surface wettability including for chemically modified surfaces.

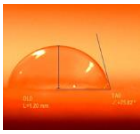
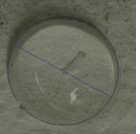
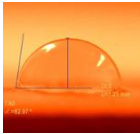
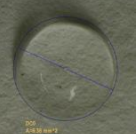
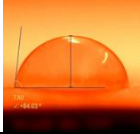
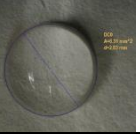
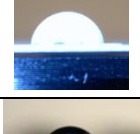
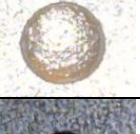

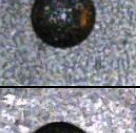
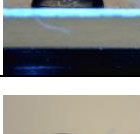
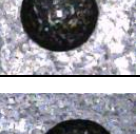
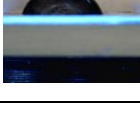

By contrast, the parafilm, which has no strongly visible surface features, is also hydrophobic with $\theta \sim (107-109)^\circ$. These results are consistent for measurements of water drops on paraffin films generally [41].

The Surface series of coatings are produced by Australian manufacturer Skycool Pty Ltd. and are intended for both improving heat insulation and water repellency of building roofing through a propriety combination of chemical and structural properties [42,43]. We were asked to perform tests on these samples to ascertain whether they were achieving the desired hydrophobicity. Of the test samples that were characterized, only three samples are found to be hydrophobic although all had contact angles above 77° .

Table 1. Comparison of three methods (tangent, spheroidal segment and top-down) for the measurement of contact angle of different surfaces and water drop volumes.

SAMPLE	DROP Volume (μL)	IMAGES		Contact Angle (θ°)		
		SIDE VIEW	TOP VIEW	SIDE		TOP
				Tangent	Spheroidal Segment	
Teflon printed G350805-BK (Polytetrafluorethylene-based polymer film on BK7 glass slide)	1.5			112-113	111	110
	2.5			113-114	114	113
	3.0			117	119	115
Teflon printed G350805-BK (Polytetrafluorethylene-based polymer film on BK7 glass slide)	3.5			118	117	117
	4.0			120	120	115
	4.5			112-113	113	112
	5.0			117-120	114	113-114
	5.5			114-115	115	113
	6.5			107	107	107
	7.5			115	111	110

SAMPLE	DROP Volume	IMAGES		Contact Angle (θ°)		
		SIDE VIEW	TOP VIEW	SIDE	TOP	
	8.0			114-117	103	106
	9.0			110	111	107
STARFROST silane coated yellow G312Si-Y hydrophobic section (BK7 glass slide – rough end)	3.5			116	118	115
STARFROST silane coated yellow G312Si-Y hydrophilic section (BK7 glass slide – smooth end)	3.5			56	56	56
STARFROST silane coated yellow G312Si-Y hydrophilic section (BK7 glass slide – smooth end)	5.0			54	53	54
	10.0			56	56	56
Parafilm (Paraffin film with paper backing)	3.5			103	104	101
Surface 94B2 (Proprietary industrial roofing film)	5.0			101	101	100
Surface 94F2 (Proprietary industrial roofing film)	5.0			107-109	107	108
Surface 94E2 (Proprietary industrial roofing film)	5.0			111	108	111

SAMPLE	DROP Volume	IMAGES		Contact Angle (θ°)		
		SIDE VIEW	TOP VIEW	SIDE	TOP	
Surface Skycool 6200-P (Proprietary reflective white paint)	5.0			77	78	77
Surface Skycool 6200-M (Proprietary reflective white paint)	5.0			82-83	83	83
Surface Skycool 6200-E (Proprietary reflective white paint)	5.0			84	83	84
Brazilian Aspen Paper (Propriety, Surface density 120 g/m ²)	4.0			84 ± 4	84 ± 4	86 ± 2
Black powdered ink laser printed Brazilian Aspen paper	4.0			107 ± 4	106 ± 4	108 ± 5
Black powdered ink laser printed Brazilian Aspen paper with organic oil (SOYA) spread on surface (50nL/mm ²)	4.0			84 ± 2	84 ± 2	83 ± 2
Black powdered ink laser printed Brazilian Aspen paper with mineral oil (UltraGear MB 80 W / API GL-4 / MB 235.1 / SAE 80 W) spread on surface (50 nL/mm ²)	4.0			72 ± 2	72 ± 2	71 ± 5

The Aspen paper used here is high quality laser printing paper with a silica nanoparticle density on the surface of 125 g/m² substantially greater than thinner, more common Aspen 30, 50 and 100 papers with 75 g/m². Interestingly, the Aspen printing paper was hydrophilic at $\theta \sim 84^\circ$ although near to 90° reflecting both surface roughness and particulate distribution - for comparison typical glass slides are very hydrophilic with $\theta \sim 27^\circ$ and $\theta < 8^\circ$ with cleaning, both chemical and laser [6]. When the paper is coated with black powdered ink during printing, that angle becomes hydrophobic at $\theta \sim 107^\circ$, in part due to the composition of the black ink which is a carbon mixed polymer. The carbon is made up of micro particles with diameters $\phi \sim 8\text{-}10 \mu\text{m}$, which aggregate on the Aspen paper to adjust roughness and give rise to the more visible granularity on the paper making it hydrophobic. Although the composition is propriety, the polymer is probably a styrene based copolymer that helps with binding the aggregates and reduces spreading of the ink. Placing organic soya or inorganic mineral oils on the printed sheet smooths out roughness and reduces the contact angle back to $\theta \sim (83\text{-}84)^\circ$ and $\theta \sim (71\text{-}72)^\circ$, respectively. With a difference $\Delta\theta \sim 12^\circ$ it is feasible to discriminate between the two types of oils based on the measured contact angle. All three methods were able to detect these changes and within reasonable experimental error are comparable.

Figures 4(a) and 4(b) summarize the median and mean contact angle data for the three methods shown in Table 1 for surfaces other than the Aspen paper. The difference between median and mean values is shown to be relatively small although it does vary noticeably between different surfaces in Fig. 4(b). When all drop volumes are considered there is a spread indicating a comparative error as high as $\Delta\theta = \pm 4^\circ$. However, when the volume is below $5 \mu\text{L}$, reducing influences arising from drop deformation, this error is reduced to $\Delta\theta = \pm 2^\circ$. Within each set of identical drop measurements $< 5 \mu\text{L}$ the variation between methods is $\Delta\theta < \pm 1^\circ$, indicating that whilst the variation between multiple measurements on a surface is sensitive to changes in surface properties. The greatest observed variations always occur for the direct tangent measurement since this requires an element of operator uncertainty in placing the tangent, worsening considerably in the hydrophobic regime $\theta \geq 90^\circ$.

When the results are analyzed in their entirety it is clear that the top-down method is robust and reliable and comparable with standard side based measurements – all three methods have average values within 2° of each other, a remarkably good agreement. Therefore, mapping wettability is demonstrably feasible and with a relatively simple algorithm it should be possible to employ low cost imaging across a sample surface and build for the first time wettability maps. To demonstrate this here we use the top-down approach to map wettability across the larger surfaces of the Aspen paper samples. Visually, the mineral oil leaves very little trace of its presence and so forms an ideal test bed for demonstrating the power of imaging wettability as a potential quality assurance measure. Such tests may have significant potential as forensic diagnostics both in detecting the presence of materials such as oils and identifying the nature of the material based on its contact angle.

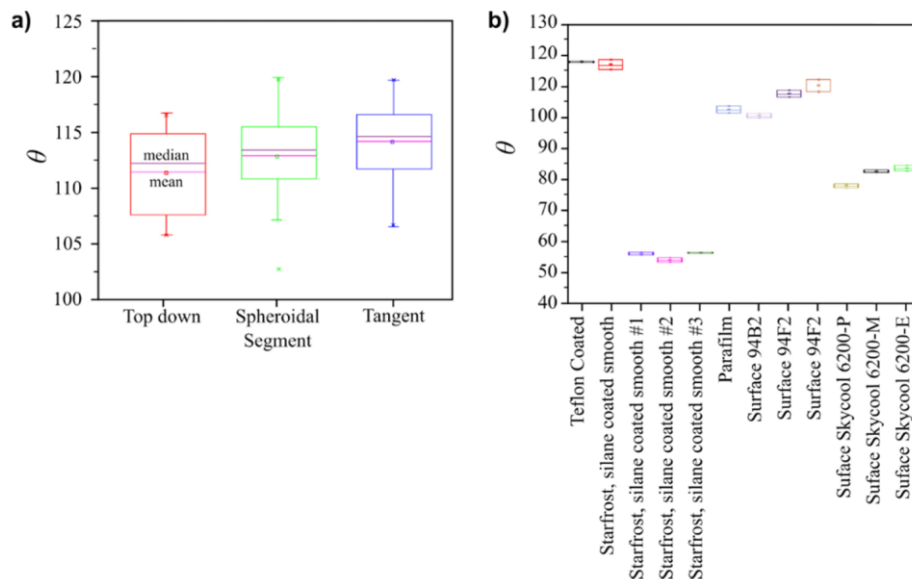


Fig. 4. Median and mean of the contact angle data measured on a test surface for reproducibility and comparison using a range of drop sizes from 1.5 to $8 \mu\text{L}$: (a) Three Teflon samples; (b) Other samples from Table 1.

2.2 Surface mapping

To demonstrate the ability to map surfaces, we first undertake a linear map across a silicon wafer slide, which has had several regions of silver (Ag) nanoparticulate droplets deposited with precisely varying dimensions from ~ 5 to 20 nm . Thermal evaporation has been refined to produce with unprecedented control a series of metal particulates of any desired size on surfaces that can be tailored for the desired surface plasmon resonances, depending on the

applications within photonics, photovoltaics and biosensing. The dimensions can be further tailored using Ar^+ beam bombardment.

Such control over surface properties means that wettability can also be tuned and this system forms an ideal test bed for the rapid application of the methods we are proposing here. Figure 5 shows an optical image of the sample and the color changes from reddish to blue to dark blue where the wafer is free of any matter. SEM images show the typical feature sizes and coverage along the length. Again for this experiment, both top-down and side measurements were undertaken simultaneously using two portable mini-microscope imaging cameras, the details are described in the methods section. Two images of the drop placed in two locations showing both top and side views give an immediate indication of the hydrophobic properties of the metal versus the hydrophilic properties of the silicon wafer (which has a thermal oxide nanolayer formed immediately after wafer fabrication). The contact angle along the length is shown as the vertical scale in n position 1 to position 4 the contact angle, measured three times, rises between $\theta = 110$ to 117° a relatively small change that is readily detected with considerable accuracy by the methods employed. The side and top-down methods are all identical within 0.5° . When the measurement is done on the bare wafer region, the contact angle drops dramatically to the approximated value expected for the thermal oxide on silicon layer $\theta = (60.5 \pm 0.5)^\circ$.

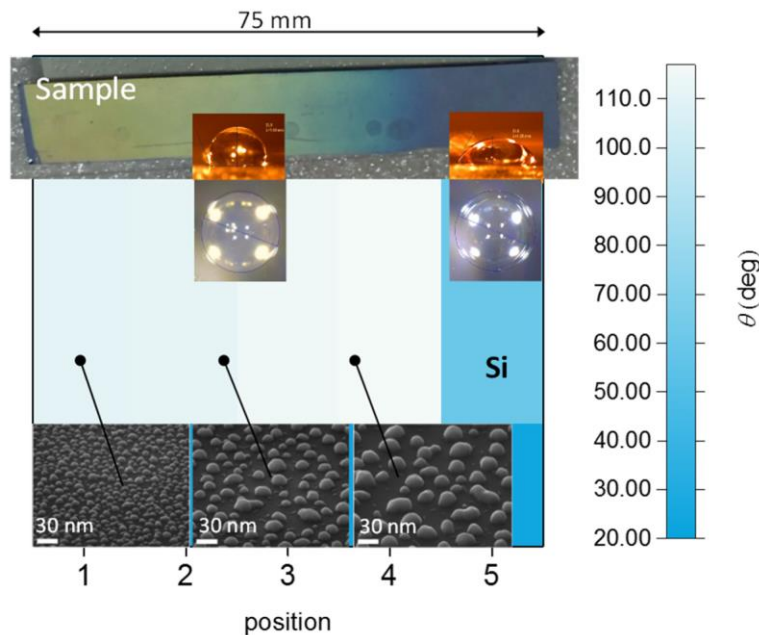


Fig. 5. Function of position along the chirped nanoparticle coated surface with increasing nanoparticle size from left to right. The density drops as the particle size increases since the thermal evaporation method involves identical amounts of Ag in each region.

The one dimensional map demonstrates high resolution and high accuracy suitable for studying nanoscale properties is possible – but it also shows that this is possible with all three methods. To explore much larger scale two dimensional mapping, impossible using the side methods, Aspen paper with large printed black areas of $(175 \times 175) \text{ mm}^2$ using a standard laser printer are used. Printing details are in the materials and methods section. This square area is sub-divided into 1225 regions of $(5 \times 5) \text{ mm}^2$. Onto each region a drop of water ($4 \pm 0.2 \mu\text{L}$; $\pm 5\%$) is deposited using a precision pipette. A top image of these drops is then taken and analyzed using the top-down method – neither side-based measurement can address the

challenge of taking measurements of drops away from the edges of the paper. The results are summarized on Fig. 6.

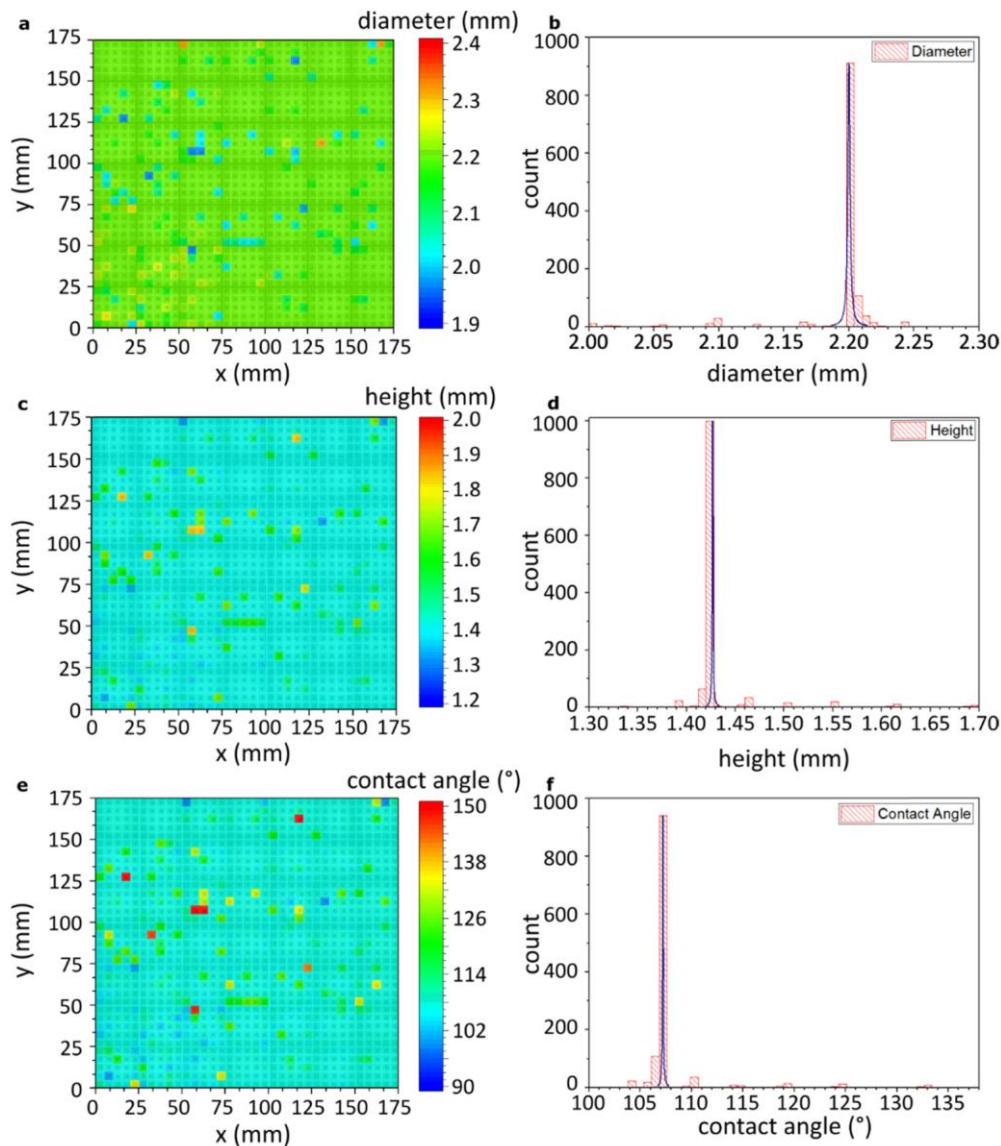


Fig. 6. (a) Mapping of diameter on a black laser printed Aspen paper; (b) Histogram and normal distribution of diameter mapping on a black laser printed Aspen paper; (c) Mapping of height on a black laser printed Aspen paper. (d) Histogram and normal distribution of height mapping on a black laser printed Aspen paper. (e) Mapping of contact angle on a black laser printed Aspen paper. (f) Histogram and normal distribution of contact angle mapping on a black laser printed Aspen paper.

In the first instance the raw measured diameters is shown in Fig. 6(a) and a histogram of this data plotted in Fig. 6(b). A diameter of $\phi = (2.19 \pm 0.03)$ mm (a variation of $\pm 2\%$ across the entire paper) is visualized and is consistent with a robust methodology as ascertained in the previous measurements. Consequently, the values lying outside this range likely show non-homogeneous printing and local defects on the paper. Similar results are obtained with the calculation of the height using the volume, shown in Fig. 6(c) and 6(d), where the height

average is estimated to be $h = (1.41 \pm 0.04)$ mm, a 3% error. Figures 6(e) and 6(f) show the maps and histograms for the calculated contact angles for comparison. The mean value for contact angle is $\theta = (108 \pm 5)^\circ$ an error of $\sim 4\%$ is finally obtained. The ability to make accurate two dimensional maps over a variable surface demonstrates the feasibility of robust, large area contact angle measurements. What is evident is that despite the printing properties and general environment of printing, the wettability obtained with ink coatings is reasonably uniform over the paper, demonstrating the suitability of this method for quality control monitoring as well as surface assessment.

To demonstrate the power of spatial mapping of contact angle and the simplicity of this method, a sample Aspen sheet was again coated with the same black powdered ink by direct laser printing. A rectangle area of (65×45) mm² is produced. This rectangle is divided into 117 regions each with an area (5×5) mm². 32 regions were then coated with the mineral oil used in Table 1 (UltraGear MB 80W - API GL-4 - MB 235.1 - SAE 80W). The volume of oil was spread using a cotton stick with no particular control in methodology employed to simulate real life uncertain contamination. All regions have a drop of water deposited on them ($V = (4 \pm 0.2)$ μ L; $\pm 5\%$) and were analyzed by the top-down method. The results are summarized in Fig. 7. Images were taken with an optical microscope (40x zoom) shown in Fig. 7(a) and 7(b) – once apparently dried, from the optical evidence alone it is not possible to distinguish the areas which have the oil to those that don't. The contact angle of the uncontaminated ink regions is as expected $\theta = 108^\circ$. However, this is reduced substantially to $\theta = (75 - 89)^\circ$ in the areas where the oil is placed. Color map visualization on top of the photographic image readily highlights the area covered with oil, revealing the acronym logo of the Brazilian Science Without Borders – Ciência sem Fronteiras (CsF) – which has supported this work. This is straightforward example of how the mapping method can be used in forensic analysis of surface properties both to discover and analyses the presence of surface contaminants, including specific chemicals. This is in addition to quality.

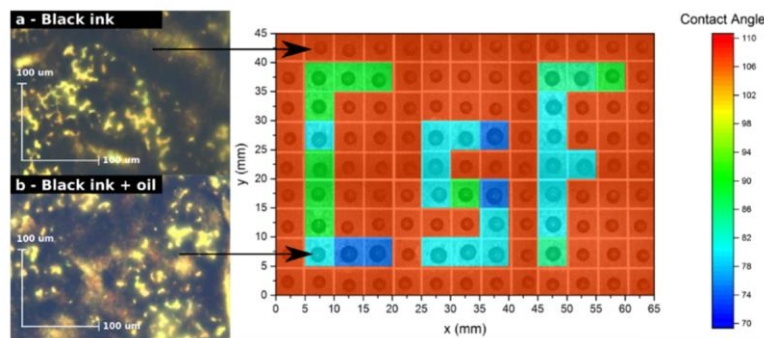


Fig. 7. Mapping of black powdered ink laser printed aspen paper contaminated with mineral oil UltraGear MB 80W. In detail (a) optical microscope image (lens 40x) of the black ink area, on (b) optical microscope image (lens 40x) of contaminated area with mineral oil.

3. Discussion

We have demonstrated the large area mapping of surface wettability by mapping the properties of solvent drops on a surface using a top-down analysis. From these properties the contact angle, a measure of the wettability, is obtained and plotted. The data can be combined with optical imaging to obtained sophisticated representation of surface features and to identify anomalous data as well as contaminants and other species. The uncertainty associated with single side measurements is removed and real time statistics is possible. The method is remarkably simple and robust comparable with all side method measurements. The potential of mapping the nanoscale interface properties of wetting over very large areas in rapid timeframes, including real time, for the first time opens up an entire new area of diagnostics,

making possible mass diagnostics for biomedical applications, mapping and quality control for industrial applications, and mass chemical analysis and studies for research and forensics and more. The simplicity of the method based on direct imaging makes it amenable to a range of wireless devices including smartphone and tablet integration, another new area of instrument research that has seen remarkable advances in areas such as hand-held IoT compatible, smart device spectroscopy and laser beam analysis [44–48].

4. Materials and methods

4.1 Top-down contact angle measurements

For the data collected in Table 1 drops are placed on each surface using an electronic micropipette of variable dispense volume $V = (0.1 - 10) \mu\text{L}$. Portable Dino-lite mini-microscope digital cameras are used to image both side and tops of each drop simultaneously as illustrated in Fig. 8. Before any measurements were taken, the microscopes were both calibrated using reference measures. The surfaces sit on an x, y and z translation stage. For the 2-D imaging, in Fig. 5 to Fig. 7, only top-down views are collected using a single portable mini-microscope digital camera. The backlight and a light diffuser contribute to improving the contrast in imaging of the droplet for side measurements. The microscopes were set at fixed magnifications and then not altered. Focusing was achieved by altering the translation stage and moving the droplet so that calibration wasn't altered. We used droplet volumes in the range $(2.0 - 10.0) \mu\text{L}$, with precision of $\pm 4\%$ and $\pm 1\%$, for the maximum and minimum volumes respectively, for since for larger droplets the drops would show visible deformation due to gravity changing the contact angle.

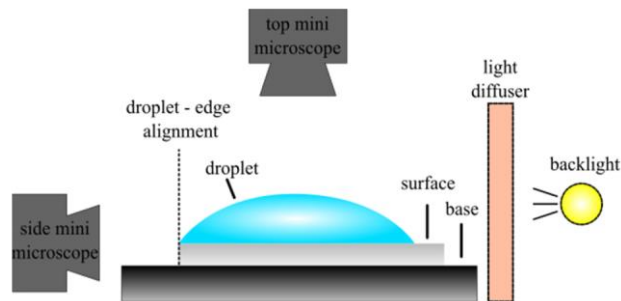


Fig. 8. Experimental setup for simultaneous side measurements (tangent and spheroidal (or height diameter) methods) and top measurement (top-down method)

For the side methods the tangent is manually measured directly using commercial software (DinoCapture 2.0) whereas the other side and top parameters are calculated from the height, volume and diameter of the drops as described in the theory earlier. The vertex of the tangent is located in the triple interface surface-droplet-air. The contact angle θ is measured between the tangent and the droplet-surface interface. Using the same program both height h and base diameter d_{cap} (or radius r_{cap}) for the spheroidal method calculation (Eq. (3)) are obtained.

Using side measurements both the omniphobic as the omniphilic case are calculated in the same way. However, using the top-down method for the omniphilic case the caplet base radius r_{cap} (or caplet base diameter, d_{cap}) is directly measured. For the omniphobic case the radius r (or diameter, d), equivalent to full sphere, is measured. The general methodology for top-down analysis and its practical approach are outlined in Table 2.

Table 2. General methodology for the top view method and your variation for practical applications

Method	Omniphilic drops	Omniphobic drops
Top-down method	<ol style="list-style-type: none"> The measured radius of the drop cap is r_{cap}; Solve the equation (6) to obtain h; Solve the equation (3) to obtain θ. 	<ol style="list-style-type: none"> The measured radius is r which is the full radius of the drop; Solve the definition of spherical cap volume to obtain h; Solve the equation (4) to obtain r_{cap}; Solve the equation (3) to obtain θ.
Practical approach	<ol style="list-style-type: none"> The measured radius of the drop cap is r_{cap}. Solve the first of Equation (6) (e.g. via smart phone app) to obtain h; Rearrange Equation (4) to determine the full radius of the drop; Calculate the volume ratio V_r, using equation (8), and then look up the contact angle from Fig. 3(a). 	<ol style="list-style-type: none"> The measured radius is r_{cap} which is also taken to be the radius of a full spherical drop; Calculate the volume ratio V_r, using equation (8) and then look up the contact angle from Fig. 3(b).

4.2 Surface mapping

Thermal evaporation of silver is used to deposit Ag nanoparticles droplets of varying size (5 – 20 nm) from one of a silicon slide cut from a wafer to the other as shown in Fig. 5. Control of the nanoparticle size was achieved using Ar ion bombardment and controlling the exposure – this generated a chirped variation along the silicon slide. The change in dimensions should lead to measurable changes in contact angle based on structural interaction at the interface with a drop.

For two dimensional mapping, in Fig. 6, a square region with (175 x 175) mm² was designed on AutoCAD (2016 – academic version) and divided into 1225 squares (35 x 35) with (5 x 5) mm² each. The patterns were colored in black (RGB: 0, 0, 0) and laser printed by Konica Minolta© bizhub PRO C6501 printer with original toners. Unlike common Aspen paper, the Aspen paper used in this work has a high surface density of 120 g/m² and is widely used in Brazil. Using a precision pipette (Labnet 2 - 20 μ L) a drop of water ($4 \pm 0.2 \mu$ L; $\pm 5\%$) is deposited manually on each region. A top image of all areas with these drops is taken, with a similar setup of Fig. 8 but using only the top mini-microscope, and analyzed using the top-down method already described.

To reveal mineral oil contamination on a surface, in Fig. 7, an area of (65 x 45) mm² was divided into 117 squares (13 x 9) with (5 x 5) mm². Similar to that described above, this area was printed in black on Aspen paper. The mineral oil was spread on the surface of 32 regions using a cotton stick forming a CsF logo. There was no control of volume in order to simulate a realistic arbitrary deposition. After drying is not possible to observe differences between regions with and without oil. Again a drop of water ($4 \pm 0.2 \mu$ L; $\pm 5\%$) is deposited manually on each region with a precision pipette. A top image is taken and analyzed by top-down method. In addition, images of regions with and without oil were examined with an optical microscope (lens 40x).

Funding

Ciência sem Fronteiras (401914/2013-5); Australian Research Council; private funding (J. Canning, W. Padden and S. Dligatch).

Acknowledgments

The authors acknowledge CsF Brazil, CNPq, CAPES, FINEP, Fundação Araucária, CSIRO and ARC.